


Cite this: *RSC Adv.*, 2021, 11, 37612

# Effect of irradiation-induced cascade mixing on spinodal decomposition in U–Nb and U–Zr alloys: a phase field study

Yong Lu,<sup>id</sup>\*<sup>a</sup> Honghao Guo,<sup>a</sup> Hengfeng Gong,<sup>c</sup> Zheng Jiang,<sup>a</sup> Xiaoyi Huang,<sup>a</sup> Xingjun Liu<sup>ab</sup> and Cuiping Wang<sup>\*ab</sup>

The spinodal decomposition of the  $\gamma$ -phase in U–Nb and U–Zr alloys under irradiation was investigated using the phase-field method coupled with micro-elasticity theory and rate dependent cascade mixing model. Microstructure evolutions of spinodal decomposition in U–Nb and U–Zr alloys were simulated by considering different initial compositions and dose rates. The volume fraction and composition distribution under different cascade mixing were presented. The simulation results show that the volume fractions and equilibrium composition of the (Nb,Zr)-rich  $\gamma_2$ -phase and the rate of spinodal decomposition are influenced by the dose rate and initial alloy composition. The cascade mixing can drive Nb or Zr atoms back into solution until a new equilibrium state between local cascade mixing and spinodal decomposition is reached. The evolution analysis indicated that irradiation-induced cascade mixing acts in opposition to thermodynamically driven spontaneous spinodal decomposition, which can not only slow down the spinodal decomposition but also reduces the composition range of the miscibility gap.

Received 1st October 2021  
Accepted 29th October 2021

DOI: 10.1039/d1ra07324a

rsc.li/rsc-advances

## 1. Introduction

Recently, uranium based metallic nuclear fuels have attracted more and more attention due to their advantages in mechanical properties, thermal conductivity and irradiation performance.<sup>1,2</sup> The body centered cubic (bcc)  $\gamma$ -phase in metallic uranium alloys is more resistant to swelling than the orthorhombic  $\alpha$ -phase under irradiation conditions. Uranium alloys with the addition of Nb greatly improves the melting point, heat transfer and swelling resistance,<sup>3,4</sup> while the addition of Zr increases the solidus temperature and stabilizes the isotropic  $\gamma$ -phase over a wider temperature range.<sup>5,6</sup> According to thermodynamic equilibrium phase diagram,<sup>7,8</sup> both of U–Nb and U–Zr alloys have continuous solid solution of  $\gamma$ -phase and miscibility gap in the high temperature region, which make it possible for the alloys to be used steadily at high temperatures. The addition of Nb and Zr can prevent oxidation of uranium<sup>9</sup> and reduce the chemical interaction of fuel-cladding.<sup>10</sup> Therefore, U–Nb and U–Zr alloys are considered the candidates of metallic nuclear fuels for next generation fast reactors.<sup>3,11</sup>

There are many efforts made to develop the U–Nb and U–Zr alloys, such as the studies of mechanical properties,<sup>12,13</sup> creep behavior,<sup>4,14</sup> and phase transformation.<sup>3</sup> Many researches have focused on spinodal decomposition in U–Nb and U–Zr alloys, which could bring miscibility gaps and heterogeneous microstructure in a large temperature region. According to Hsiung *et al.*'s<sup>15</sup> study and Clarke *et al.*'s<sup>16</sup> experimental results, the nanoscale modulation caused by the spinodal decomposition can lead to the age hardening and make good stability at low temperatures in U–Nb alloys. Studying the microstructure of irradiated annular U–Zr fuel by microscopic multi-scale characterization, Yao *et al.*<sup>17,18</sup> found that the alloy formed nanoscale spinodal decomposition microstructure after irradiation, which could effectively prevent radiation swelling of fuel slug. Thus, it is essential to study the spinodal decomposition in metallic nuclear fuels under irradiation.

As good candidates for nuclear fuels, U–Nb and U–Zr alloys are exposed to the extreme environment of intense irradiation and high temperature inevitably. Previous studies have showed that irradiation impact microstructure changes of alloys through two main mechanisms: irradiation-induced mixing and irradiation-enhanced diffusion,<sup>19,20</sup> both of which could be investigated by phase-field method. There are plenty of researchers have studied the microstructure evolution under irradiation by using the phase-field method and achieved successful applications, such as gas bubble growth,<sup>21–24</sup> composition segregation,<sup>25–28</sup> grain growth<sup>29–31</sup> and so on. A

<sup>a</sup>College of Materials, Fujian Provincial Key Laboratory of Materials Genome, Xiamen University, Xiamen, 361005, PR China. E-mail: luyong@xmu.edu.cn; wangcp@xmu.edu.cn

<sup>b</sup>Department of Materials Science and Engineering, Harbin Institute of Technology, Shenzhen, 518055, PR China

<sup>c</sup>Nuclear Fuel and Materials Department, China Nuclear Power Technology Research Institute Co., Ltd, Shenzhen, 518000, PR China



phase-field model with irradiation effect proposed by Dilles *et al.*<sup>32</sup> and successfully predicted the formation of various microstructures related to spinodal hardening in Ag–Cu alloy, which provided a new perspective for the improvement of mechanical properties of alloys. Ke *et al.*<sup>33</sup> established a phase-field model for the microstructure evolution of Fe–Cr coupling with the cascade mixing model, which verified the consistency between the simulation and experimental results. The phase-field model with micro-elastic theory has also achieved success due to the application of the Khachaturyan–Shatalov theory,<sup>34,35</sup> which fully describes the inhomogeneity of structure and its spatial distribution in the mesoscopic scale. Recently, Yan *et al.*<sup>36</sup> have successfully carried out a phase-field model coupling with micro-elastic theory to study the interstitial atom and vacancy evolution in Fe–Cr alloys. Therefore, it is feasible and necessary to investigate the spinodal decomposition behavior of U–Nb and U–Zr systems under irradiation based on the phase-field method.

In the present study, based on the thermodynamic database, we have employed Cahn–Hilliard-type phase-field simulations combined with cascade mixing model to investigate the spinodal decomposition of  $\gamma$ -phase in U–Nb and U–Zr alloys under irradiation. Since the spinodal decomposition is a form of solid phase transition, we also consider the elastic energy in the phase-field model. In an attempt to find out the influence of irradiation on spinodal decomposition, different composition of U–Nb and U–Zr alloys have been studied.

## 2. Simulation methods

### 2.1 Phase-field model

To study the evolution of spinodal decomposition in U–Nb and U–Zr alloys, we have employed the phase-field model developed originally by Cahn and Hilliard.<sup>37</sup> The total free energy  $F$  of the U–Nb and U–Zr alloys includes the chemical free energy, the interfacial gradient energy and the elastic strain energy. The total free energy can be expressed as:<sup>38</sup>

$$F = \int_V \left\{ G_{\text{chem}} + \frac{1}{2} \kappa (\nabla c)^2 \right\} dV + E_{\text{el}} \quad (1)$$

where,  $c$  is the molar fraction of species Nb or Zr,  $\kappa$  is the gradient energy coefficient and  $E_{\text{el}}$  is the elastic strain energy of U–Nb or U–Zr alloy. The chemical free energy of  $\gamma$ -phase in U–Nb and U–Zr alloys can be obtained by  $G_{\text{chem}} = G^{\text{m}}/V_{\text{m}}$ , in which  $V_{\text{m}}$  is the molar volume,  $G^{\text{m}}$  is the molar Gibbs free energy and can be expressed with the regular solution model:

$$G^{\text{m}} = \sum_{i=A,B} {}^0G_i^{\gamma} c_i + RT \sum_{i=A,B} c_i \ln c_i + c_A c_B \sum_{j=0}^n {}^jL_{A,B}^{\gamma} (c_A - c_B)^j \quad (2)$$

where  ${}^0G_i^{\gamma}$  is the molar Gibbs free energy of pure  $i$  constituent element in the  $\gamma$ -phase, which is taken from the SGTE database compiled by Dinsdale.<sup>39</sup> The  $c_i$  is the atomic fraction of species  $i$  and  ${}^jL_{A,B}^{\gamma}$  is the temperature-dependent interaction parameters in the binary system which can be described as:

$${}^jL_{A,B}^{\gamma} = a_j + b_j T \quad (3)$$

Here  $a_j$  and  $b_j$  are optimized parameters. The thermodynamic data in eqn (3) are obtained from the U–Nb and U–Zr thermodynamic assessment.<sup>7,40</sup> The governing equations describing the spatial and temporal evolutions of composition is determined by the Cahn–Hilliard-type equation with a forced mixing term:<sup>33</sup>

$$\frac{\partial c}{\partial t} = \nabla \cdot \left( M \nabla \left( \frac{\partial G_{\text{chem}}}{\partial c} - \kappa \nabla^2 c + \frac{\delta E_{\text{el}}}{\delta c} \right) \right) + \frac{\partial c}{\partial t} \Big|_{\text{mixing}} \quad (4)$$

where the first term at the right side in the equation accounts for thermal diffusion driven by the gradient of diffusion potential and the second term corresponds to the cascade mixing contribution of damage cascades. The chemical mobility  $M$  is defined by Darken's equation:<sup>41</sup>

$$M = c(1 - c)[cM_{\text{U}} + (1 - c)M_{\text{i}}], \quad (\text{i} = \text{Nb or Zr}) \quad (5)$$

where  $M_{\text{U}}$ ,  $M_{\text{Nb}}$  and  $M_{\text{Zr}}$  are the atomic mobilities of U, Nb and Zr, respectively. They are related to the diffusivity through Einstein's relation  $M_i = D_i/RT$ , where  $i$  denotes the elements of U, Nb or Zr.  $R$  is the gas constant,  $T$  is the absolute temperature, and  $D_i$  is the intrinsic diffusion coefficient which can be seen in the Table 1.<sup>42,43</sup>

The continuum atom relocation model which is used in our simulation was developed by Enrique and Bellon to treat cascade mixing, in which the finite-range atomic replacements in displacement cascades is considered,<sup>44</sup> and the model was proved to be feasible by Ke *et al.*<sup>33</sup> Changes of the local component which is caused by the forced cascade mixing can be expressed as:

$$\frac{\partial c}{\partial t} \Big|_{\text{mixing}} = -\Gamma(c - \langle c \rangle_{R_L}) \quad (6)$$

Here  $\Gamma$  is the reorientation frequency which has a relationship to the irradiation displacement rate by  $b\Phi$ , where  $b$  is the parameter that represents the number of substitutions per atomic displacement,  $\Phi$  is the irradiation displacement rate,<sup>44,45</sup> and  $\langle c \rangle_{R_L}$  is the non-local mean value of concentration which is weighted by the normalized function:

$$\langle c \rangle_{R_L} = \int \omega_{R_L}(\mathbf{r} - \mathbf{r}') c(\mathbf{r}') d\mathbf{r}' \quad (7)$$

and  $\omega_{R_L}$  is the normalized function, which can be expressed by a Gaussian distribution, describing the distribution of atomic reorientations.<sup>46</sup> It can be characterized as:

$$\omega_{R_L}(\mathbf{r} - \mathbf{r}') = \left( \frac{3}{2\pi R_L^2} \right)^{\frac{3}{2}} \exp \left( -\frac{3|\mathbf{r} - \mathbf{r}'|^2}{2R_L^2} \right) \quad (8)$$

Here,  $\mathbf{r}$  represents the spatial location and  $R_L$  corresponds to the average jump distance during repositioning. In the model, the characteristics of cascades and the types of high-energy particles decide the value of  $R_L$  and  $b$ . The value of  $R_L$  is typically approximated as the average interatomic distance in bcc-lattice.<sup>47</sup> In consideration of atomic displacement without creating Frenkel pairs during the cool-down of cascades, the number of substitutions is expected to be larger than the estimated value in the model proposed by Norgett *et al.*<sup>48</sup> The value



Table 1 Parameters for the simulations

Parameters	Symbols	Values	Ref.
Gradient energy coefficient	$\kappa$	$1.8 \times 10^{-14} \text{ (mol m}^2\text{) J}^{-1}$ (In U-Nb) $0.5 \times 10^{-15} \text{ (mol m}^2\text{) J}^{-1}$ (In U-Zr)	55
Intrinsic diffusion coefficient of U	$D_U$	$9.1 \times 10^{-13} \exp\left(\frac{-48\,000 \text{ J mol}^{-1}}{RT}\right) \text{ m}^2 \text{ s}^{-1}$	42
Intrinsic diffusion coefficient of Nb	$D_{Nb}$	$3.34 \times 10^{-10} \exp\left(\frac{-106\,800 \text{ J mol}^{-1}}{RT}\right) \text{ m}^2 \text{ s}^{-1}$	42
Intrinsic diffusion coefficient of Zr	$D_{Zr}$	$5.1 \times 10^{-13} \exp\left(\frac{-51\,000 \text{ J mol}^{-1}}{RT}\right) \text{ m}^2 \text{ s}^{-1}$	43
Lattice parameters of U	$a_U$	0.343 nm	52
Lattice parameters of Nb	$a_{Nb}$	0.330 nm	54
Lattice parameters of Zr	$a_{Zr}$	0.357 nm	53
Gas constant	$R$	$8.314 \text{ J mol}^{-1} \text{ K}^{-1}$	This work
Grid length	$l$	$3.37 \times 10^{-10} \text{ m}$ (in U-Nb) $3.50 \times 10^{-10} \text{ m}$ (in U-Zr)	52–54
Elastic constant of $\gamma$ -U	$C_{ij}$	$C_{11} = 111.0 \text{ GPa}$ , $C_{12} = 117.0 \text{ GPa}$ , $C_{44} = 15.0 \text{ GPa}$	52
Elastic constant of pure Nb	$C_{ij}$	$C_{11} = 246.5 \text{ GPa}$ , $C_{12} = 134.5 \text{ GPa}$ , $C_{44} = 28.7 \text{ GPa}$	54
Elastic constant of $\beta$ -Zr	$C_{ij}$	$C_{11} = 86.6 \text{ GPa}$ , $C_{12} = 92.3 \text{ GPa}$ , $C_{44} = 26.6 \text{ GPa}$	53
Replacements per displacement	$b$	50	33 and 56
Average relocation distance	$R_L$	$3.37 \times 10^{-10} \text{ m}$ (In U-Nb) $3.50 \times 10^{-10} \text{ m}$ (In U-Zr)	52–54
Time steps	$\Delta t^*$	0.005 s	This work

of  $b$  ranges from  $\sim 1$  for electrons to  $\sim 30$ – $100$  for neutrons and heavy ions.<sup>49,50</sup> The results of this study are not highly sensitive to the specific value of  $b$  and the effect of changing the primary dose rate is less than an order of magnitude. In the simulation, the values of  $R_L$  and  $b$  for neutron/heavy-ion irradiations are chosen in Table 1.

## 2.2 Elastic energy model

The elastic strain induced by composition inhomogeneity and lattice mismatch in U–Nb and U–Zr alloys can be written as:

$$\varepsilon_{ij}^{\text{el}} = \varepsilon_{ij} - \varepsilon_{ij}^0 \quad (9)$$

and the stress free strain  $\varepsilon_{ij}^0$  can be expressed as:

$$\varepsilon_{ij}^0 = \delta_{ij} \varepsilon_0 \quad (10)$$

where  $\delta_{ij}$  is the Kronecker–Delta function,  $\varepsilon_0 = 1/a_0(da/dc)$  is the lattice expansion coefficient, in which  $a_0$  and  $a$  are the average lattice constant and the lattice constant of the alloy with composition  $c$ . The total strain  $\varepsilon_{ij}$  can be expressed as:

$$\varepsilon_{ij} = \frac{1}{2} \left( \frac{\partial u_i}{\partial x_j} + \frac{\partial u_j}{\partial x_i} \right) \quad (11)$$

Here  $u_i$  and  $u_j$  is the  $i$ th and  $j$ th composition of the displacement, respectively. According to the Hook's law, the stress  $\sigma_{ij}$  can be written as a function of elastic strain:  $\sigma_{ij} = C_{ijkl} \varepsilon_{kl}^{\text{el}}$ , where  $C_{ijkl}$  is the elastic modulus tensor. The elastic strain energy related to the configuration can be described in the reciprocal space:<sup>51</sup>

$$E_{\text{el}} = \frac{1}{2} \int \left\{ \frac{d^3 k}{(2\pi)^3} \left[ B(\mathbf{n}) |\tilde{c}(\mathbf{k})|^2 \right] \right\} \quad (12)$$

where  $\mathbf{k}$  denotes the Fourier wave vector,  $\tilde{c}(\mathbf{k})$  is the Fourier transform of composition  $c$ , and the integral  $\int$  in the infinite reciprocal space is evaluated as a principal value excluding a volume  $(2\pi)^3/V$  around the point  $\mathbf{n} = 0$ . And  $B(\mathbf{n})$  is the elastic interaction energy which can be described as:

$$B(\mathbf{n}) = C_{ijkl} \varepsilon_{ij}^0 \varepsilon_{kl}^0 - n_i \sigma_{ij}^0 \Omega_{jk}(\mathbf{n}) \sigma_{kl}^0 n_l \quad (13)$$

in the expression,  $\mathbf{n} = \frac{\mathbf{k}}{|\mathbf{k}|}$  represents a unit vector in reciprocal space,  $\Omega_{jk}(\mathbf{n})$  is the Green tensor which is inverse to the tensor  $C_{ijkl} n_k n_l$ .

## 2.3 Numerical method

In the simulation, the composition evolution equation can be obtained by substituting eqn (6) into eqn (4). For the convenience of numerical calculation, the composition evolution equation can be converted to a dimensionless form which can be expressed as:

$$\frac{\partial c^*}{\partial t^*} = \nabla^* \left( M^* \nabla^* \left( \frac{\partial G_{\text{chem}}^*}{\partial c^*} - \kappa^* (\nabla^*)^2 c^* + \frac{\delta E_{\text{el}}^*}{\delta c^*} \right) \right) - \Gamma^* \left( c^* - \langle c^* \rangle_{R_L^*} \right) \quad (14)$$

where  $t^* = \frac{t\bar{D}}{l^2}$ ,  $\nabla^* = l\nabla$ ,  $M^* = \frac{RTM}{\bar{D}}$ ,  $G_{\text{chem}}^* = \frac{V_m G_{\text{chem}}}{RT}$ ,  $\kappa^* = \frac{\kappa}{RTl^2}$ ,  $E_{\text{el}}^* = \frac{V_m E_{\text{el}}}{RT}$ ,  $\Gamma^* = \frac{\Gamma l^2}{\bar{D}}$ ,  $V_m = \frac{N_A a^3}{2}$ ,  $\bar{D} = c_U D_U + c_i D_i$ , ( $i$





= Nb or Zr).  $l$  is the grid length which is chosen as the average lattice parameter of U and Nb, or U and Zr for  $c = 0.5$ , and the dimensionless grid size is  $\Delta x^* = \Delta y^* = 1.0$ . The simulation cell is  $256\Delta x^* \times 256\Delta y^*$  and  $\Delta t^*$  is the dimensionless time steps.  $N_A$  is the Avogadro constant, and  $\bar{D}$  represents the average inter-diffusion coefficient of U-Nb or U-Zr alloy which depends on

the temperature  $T$  and the concentration of Nb or Zr, and can be calculated with the intrinsic diffusion coefficients in the Table 1. At 973 K, the calculated values of  $\bar{D}$  are  $1.96 \times 10^{-15} \text{ m}^2 \text{ s}^{-1}$  in U-45 at% Nb alloy and  $2.04 \times 10^{-15} \text{ m}^2 \text{ s}^{-1}$  in U-25 at% Zr alloy. The lattice parameters  $a_i$  ( $i = \text{U, Nb or Zr}$ ) and anisotropy elastic constants  $C_{ij}$  of  $\gamma$ -U, pure Nb and  $\beta$ -Zr are shown in the Table

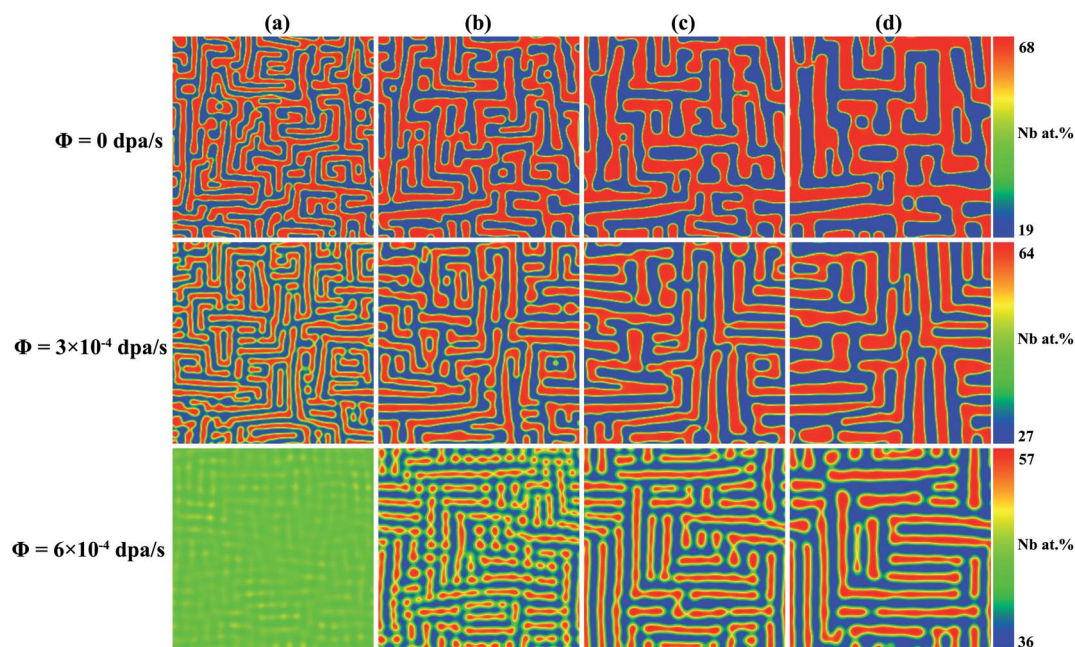


Fig. 1 Phase-field simulations of the spinodal decomposition of the  $\gamma$ -phase in U-45 at% Nb alloy at 973 K under different dpa rates: (a)  $t = 56 \text{ s}$ ; (b)  $t = 142 \text{ s}$ ; (c)  $t = 284 \text{ s}$ ; (d)  $t = 568 \text{ s}$ .

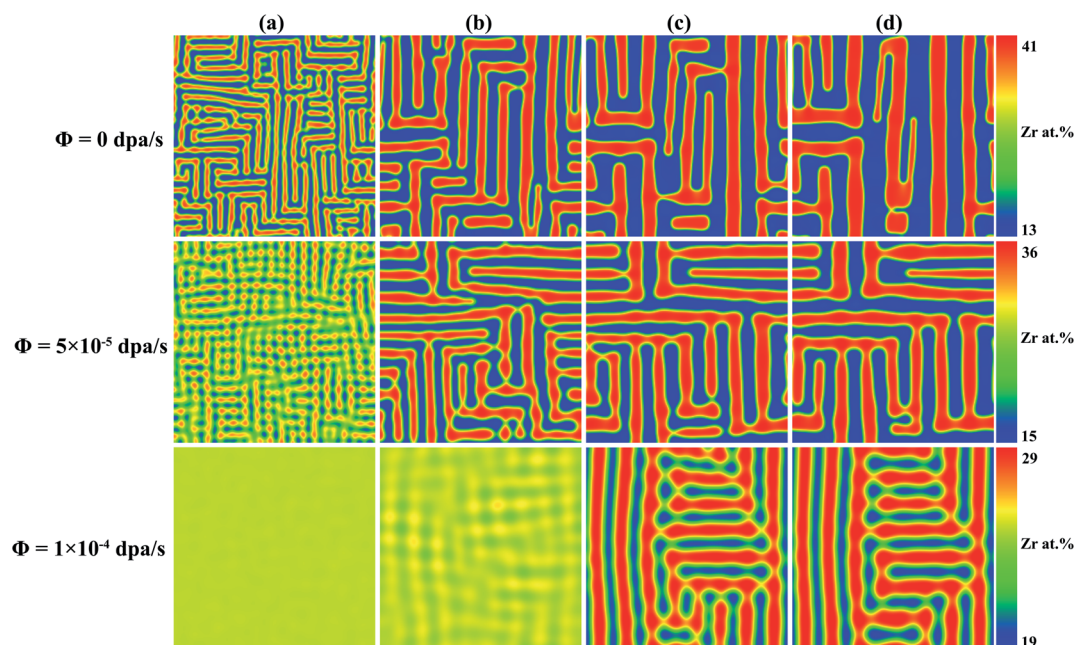


Fig. 2 Phase-field simulations of the spinodal decomposition of the  $\gamma$ -phase in U-25 at% Zr alloy at 973 K under different dpa rates: (a)  $t = 327 \text{ s}$ ; (b)  $t = 3272 \text{ s}$ ; (c)  $t = 8180 \text{ s}$ ; (d)  $t = 12 270 \text{ s}$ .





1.<sup>52–54</sup> Eqn (14) is discretized in 2-D space with a uniform grid and solved by using an explicit finite difference scheme with forward Euler time-stepping under periodic boundary conditions. The crystallographic orientation of the simulated region was determined to be [10] in horizontal direction and [01] in vertical direction.

### 3. Results

#### 3.1 Effect of irradiation on spinodal decomposition of $\gamma$ -phase

In present work, the spinodal decomposition of U–Nb and U–Zr alloys located in relative high temperature regions ( $>900$  K) and we incorporated the continuum treatment of ballistic events by Enrique and Bellon<sup>44,57</sup> into our model, which was previously used to study compositional patterning and phase stability under irradiation. According to the phase diagram of U–Nb and U–Zr alloys,<sup>7,8</sup> the miscibility gaps of Nb component in U–Nb alloys and Zr component U–Zr alloys range from 0.14 to 0.7 and 0.13 to 0.42, respectively. The spinodal decomposition behavior

in the composition range is mainly studied in this work. In our simulation, the effect of irradiation dose rate on the spinodal decomposition and microstructure evolution of different Nb or Zr component in U–Nb and U–Zr alloys at 973 K have been studied.

In order to study the effect of irradiation on the microstructure evolution, the spinodal decomposition of  $\gamma$ -phase in U-45 at% Nb alloy at 973 K with  $0 \text{ dpa s}^{-1}$ ,  $3 \times 10^{-4} \text{ dpa s}^{-1}$  and  $6 \times 10^{-4} \text{ dpa s}^{-1}$  were simulated. As shown in Fig. 1, the temporal simulation results for 56, 142, 284 and 568 s were labeled by (a) to (d). The dark red regions are the Nb or Zr enriched  $\gamma_2$ -phase, and the dark blue regions denote the U enriched  $\gamma_1$ -phase. It can be seen that two-phase microstructure gradually appears as the simulation time increases. The size of  $\gamma_2$ -phase decreases and the microstructure evolution in U–Nb alloy slows down with the increase of dose rates. Fig. 2 shows the time evolution of spinodal decomposition of  $\gamma$ -phase in U-25 at% Zr alloy with  $0 \text{ dpa s}^{-1}$ ,  $5 \times 10^{-5} \text{ dpa s}^{-1}$  and  $1 \times 10^{-4} \text{ dpa s}^{-1}$ , and the columns of (a) to (d) indicate simulation results of 327, 3272, 8180 and 12 270 s, respectively. The spinodal decomposition evolves along the vertical and horizontal directions and the phase fraction of Zr enriched  $\gamma_2$ -phase

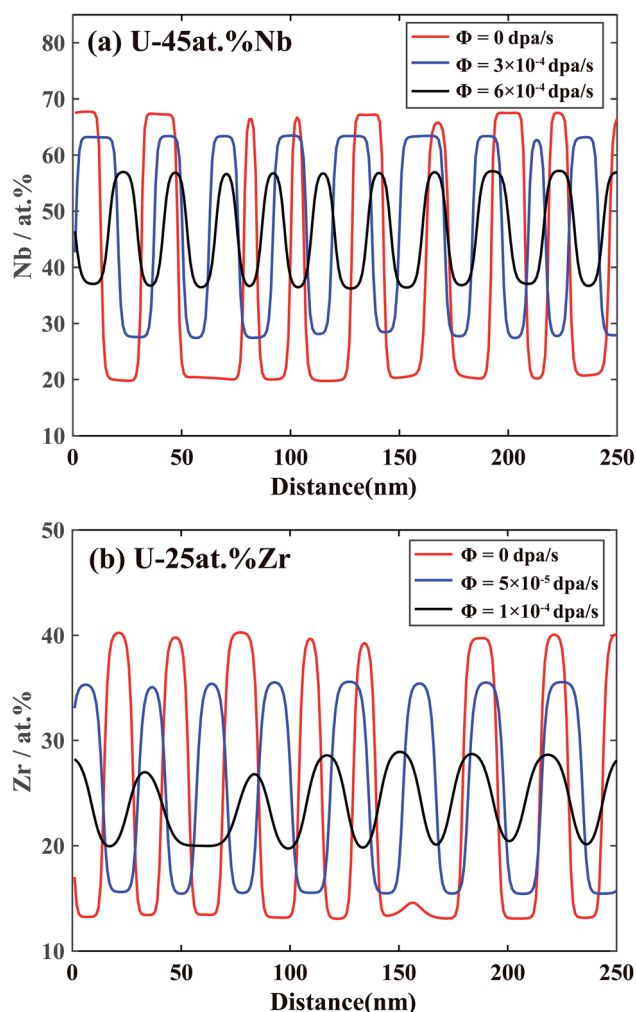


Fig. 3 Profile of solute compositions at 973 K under different dpa rates: (a) U-45 at% Nb and (b) U-25 at% Zr.

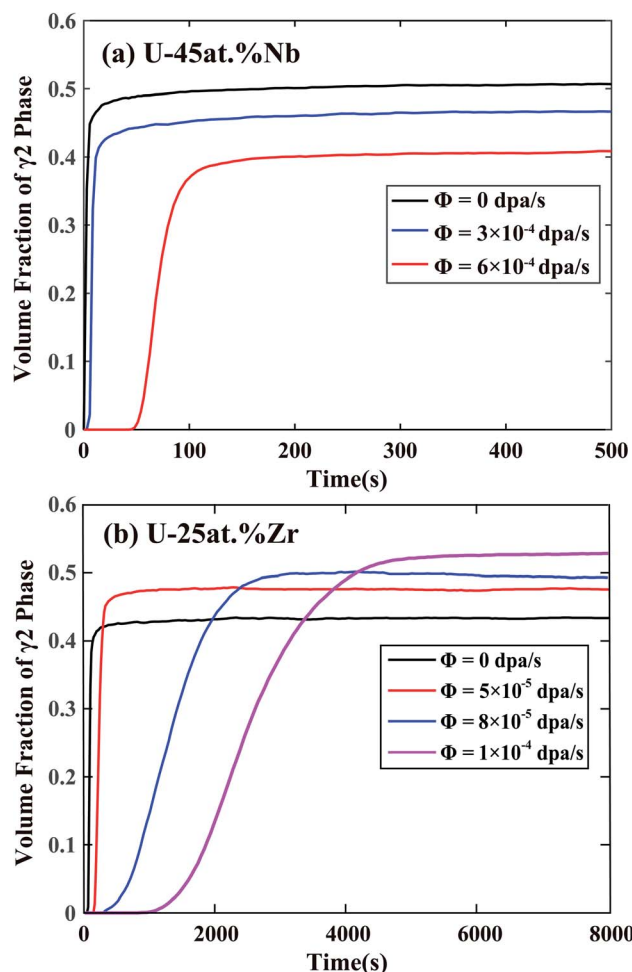


Fig. 4 The volume fraction variation of  $\gamma_2$ -phase as a function of time under different dpa rates: (a) U-45 at% Nb and (b) U-25 at% Zr.



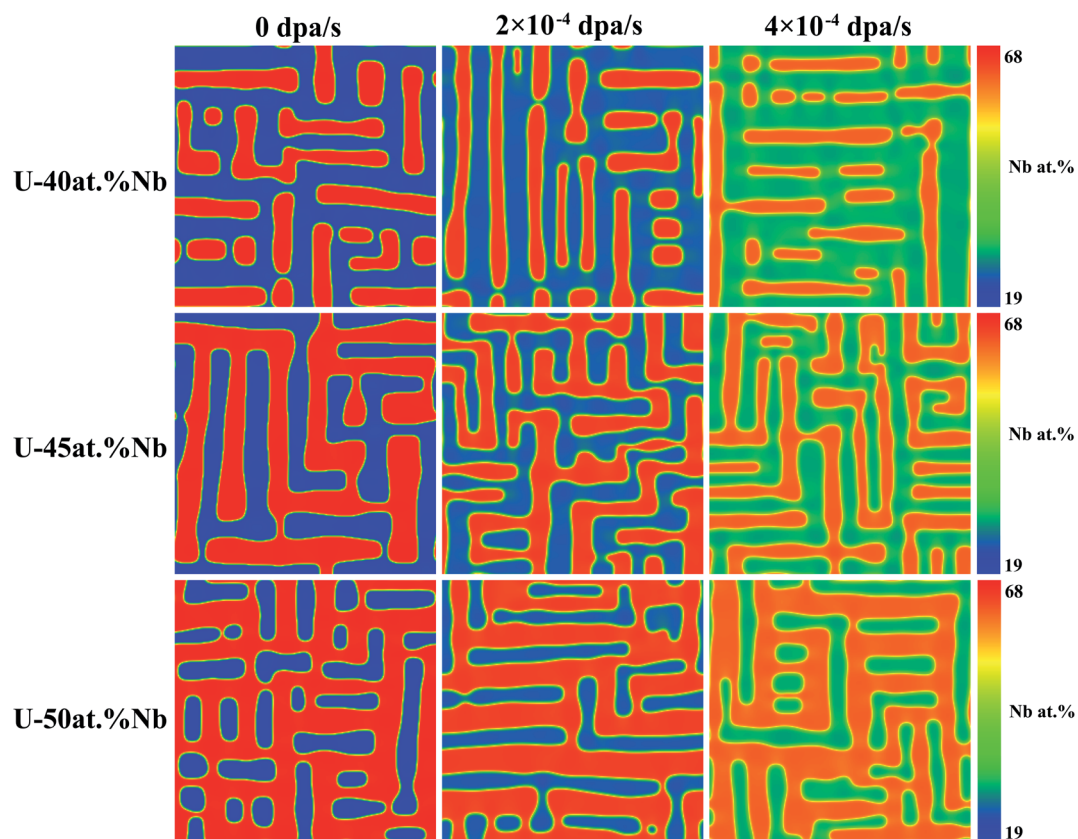


Fig. 5 Morphology of U–Nb alloy at 973 K under different dpa rates and initial compositions.

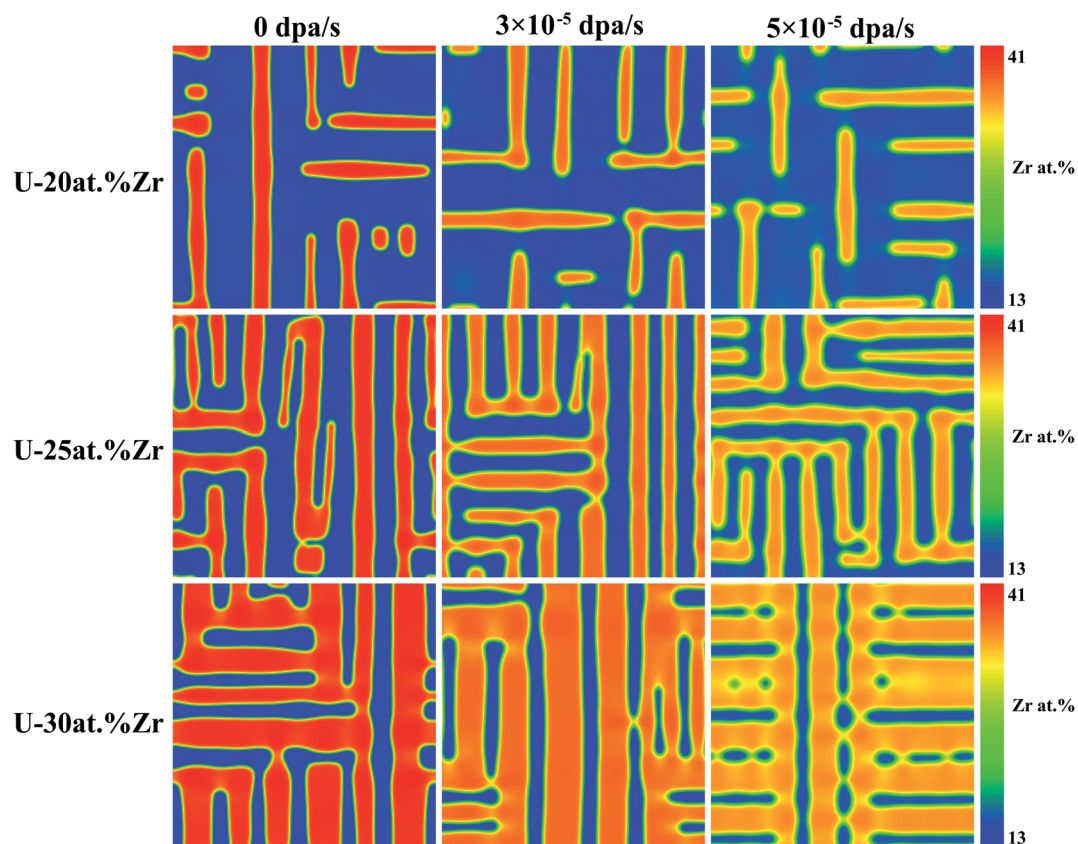


Fig. 6 Morphology of U–Zr alloy at 973 K under different dpa rates and initial compositions.



increases with the increase of dose rates in the Fig. 2. The simulation results indicate that the elastic energy could have great influence on the anisotropy of the microstructure morphology.

The compositions–distance curves of  $\gamma_1$  and  $\gamma_2$ -phase under different dpa rate in U-45 at% Nb alloy and U-25 at% Zr alloy were plotted in Fig. 3(a) and (b), respectively. One can easily find that the  $\gamma_1$  and  $\gamma_2$ -phase in U-45 at% Nb alloy can reach equilibrium compositions of 0.19 and 0.68 without irradiation, while reducing to equilibrium compositions of 0.36 and 0.57 under the dpa rate of  $6 \times 10^{-4}$  dpa s $^{-1}$ . The  $\gamma_1$ -phase and  $\gamma_2$ -phase in U-25 at% Zr alloy can reach equilibrium compositions of 0.13 and 0.41 without irradiation, while reducing to equilibrium compositions of 0.20 and 0.29 under the dpa rate of  $1 \times 10^{-4}$  dpa s $^{-1}$ . In the simulation,  $\Delta c^{\text{eq}} = |c_1^{\text{eq}} - c_2^{\text{eq}}|$  indicates the width of the miscibility gap in the equilibrium phase diagram, where  $c_1^{\text{eq}}$  and  $c_2^{\text{eq}}$  are the average equilibrium compositions of Nb or Zr-lean and Nb or Zr-rich phases, respectively. The width of the miscibility gap  $\Delta c^{\text{eq}}$  in U-45 at% Nb alloy is 0.49 without irradiation, while  $\Delta c^{\text{eq}} = 0.21$  under the dpa rate of  $6 \times 10^{-4}$  dpa s $^{-1}$ . In U-25 at% Zr alloy,  $\Delta c^{\text{eq}} = 0.28$  without irradiation, while  $\Delta c^{\text{eq}} = 0.09$  under the dpa rate of  $1 \times 10^{-4}$  dpa s $^{-1}$ . As can be seen from the figures, the width of miscibility gap for both of the U–Nb and U–Zr shrink with the increase of dose rates.

As referred above, the irradiation-induced cascade mixing can influence the equilibrium composition of two phases after spinodal decomposition. Furthermore, in order to clarify the effects of irradiation on the speed of spinodal decomposition, the variations of  $\gamma_2$ -phase volume fractions as a function of time under different dose rates in U-45 at% Nb and U-25 at% Zr alloys were plotted in Fig. 4(a) and (b), respectively. It is seen that, without irradiation, the volume fractions of  $\gamma_2$ -phase are able to reach the equilibrium values of 0.50 and 0.42 for U-45 at% Nb and U-25 at% Zr alloys, respectively. As the dose rate increases, it takes longer time for the  $\gamma_2$ -phase to reach the equilibrium volume fractions. In addition, the increase of dose rates results in a decrease of volume fraction of the  $\gamma_2$ -phase in U-45 at% Nb alloy (e.g. from 0.50 to 0.40) and an increase of volume fraction of the  $\gamma_2$ -phase in U-25 at% Zr alloy (e.g. from 0.42 to 0.52).

### 3.2 Effect of initial alloy composition on spinodal decomposition of U–Nb and U–Zr under irradiation

To investigate the influences of initial composition on spinodal decomposition under irradiation, the U–Nb and U–Zr alloys with different initial composition were simulated by phase-field method, and the results were shown in Fig. 5 and 6. Fig. 5 shows the morphologies of spinodal decomposition of U-40 at% Nb, U-45 at% Nb and U-50 at% Nb alloys under different dpa rates of 0 dpa s $^{-1}$ ,  $2 \times 10^{-4}$  dpa s $^{-1}$  and  $4 \times 10^{-4}$  dpa s $^{-1}$ . The simulation temperature is 973 K and the time  $t = 1000$  s. Fig. 6 shows the spinodal decomposition morphology of U-20 at% Zr, U-25 at% Zr and U-30 at% Zr alloys under different dpa rates of 0 dpa s $^{-1}$ ,  $3 \times 10^{-5}$  dpa s $^{-1}$  and  $6 \times 10^{-5}$  dpa s $^{-1}$ , the simulation temperature is 973 K and the time  $t = 10000$  s. It can be seen that, without irradiation, the phase fraction of in U–Nb and U–Zr alloys increases with the increase of Nb or Zr initial

composition. The matrix phase is U enriched  $\gamma_1$ -phase and the isolated phase is Nb or Zr enriched  $\gamma_2$ -phase in U-40 at% Nb and U-20 at% Zr alloy. When the initial alloy composition increase to 45 at% Nb and 25 at% Zr, the U enriched  $\gamma_1$ -phase and the Nb or Zr enriched  $\gamma_2$ -phase are interconnected. For U-50 at% Nb and U-30 at% Zr, the matrix phase is  $\gamma_2$ -phase and the isolated phase is U enriched  $\gamma_1$ -phase. It can be noticed that the favorite growth direction in the two alloys remain unchanged during spinodal decomposition with the increase of dose rates.

Fig. 7(a) and (b) show the change of  $\gamma_2$ -phase volume fraction as a function of simulation time under different initial composition and dose rates for U–Nb and U–Zr alloys, respectively. The red, blue, and black color of lines represent different initial compositions and the types of lines represent different dose rates. As can be seen in Fig. 7, the volume fraction of the  $\gamma_2$ -phase quickly increases to its equilibrium value for all initial compositions without irradiation and the final volume fraction of the  $\gamma_2$ -phase increases with the increase of the initial Nb or Zr

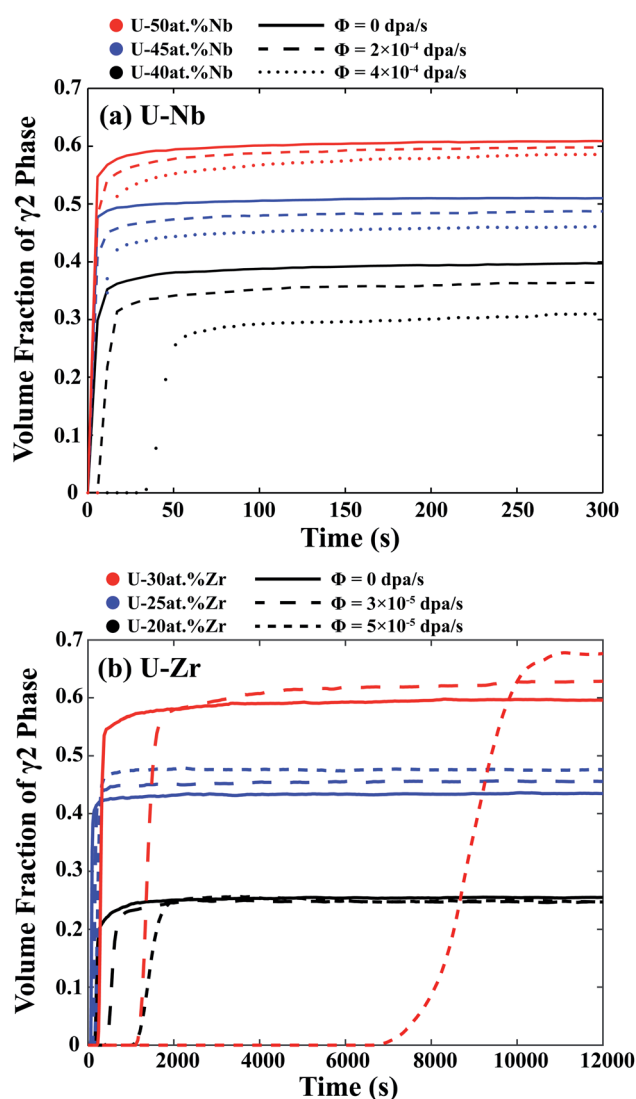


Fig. 7 The volume fraction variation of  $\gamma_2$ -phase as a function of time for different dpa rates and compositions. (a) U–Nb, (b) U–Zr.





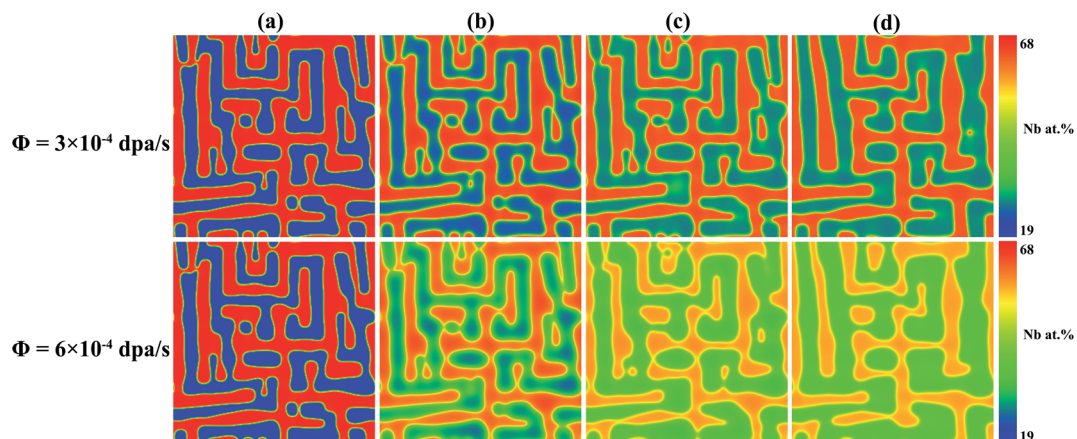


Fig. 8 Effect of irradiation on the evolution of two-phase microstructure for U-45 at% Nb alloys at 973 K: (a)  $t = 0$  s; (b)  $t = 5$  s; (c)  $t = 28$  s; (d)  $t = 284$  s.

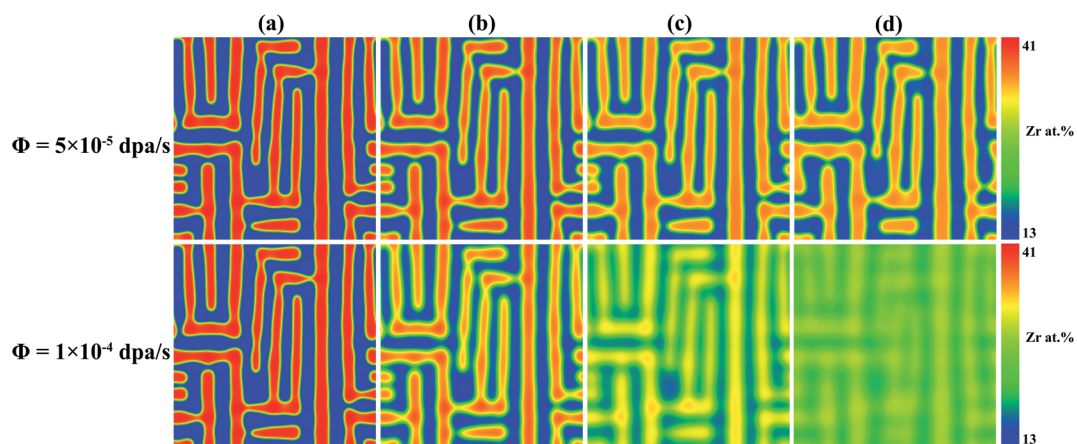


Fig. 9 Effect of irradiation on the evolution of two-phase microstructure for U-25 at% Zr alloys at 973 K: (a)  $t = 0$  s; (b)  $t = 32$  s; (c)  $t = 163$  s; (d)  $t = 1636$  s.

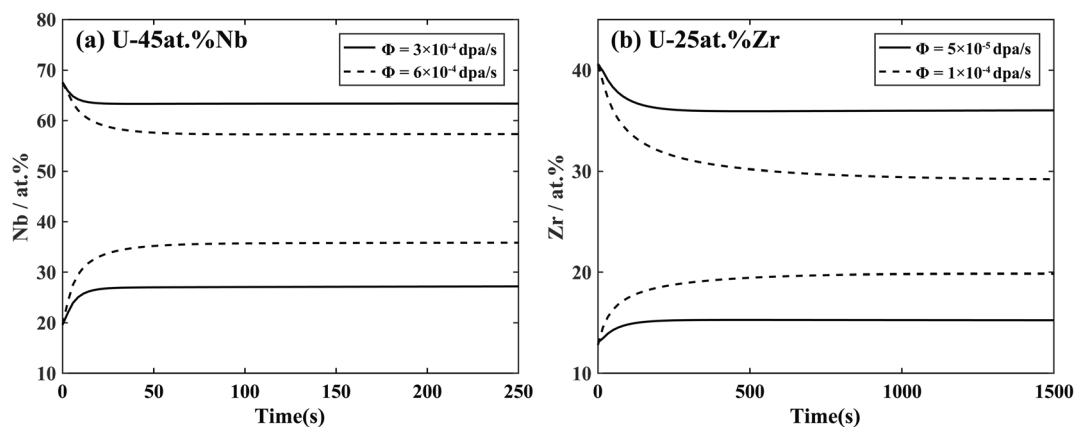


Fig. 10 Composition evolution of  $\gamma_1$ -phase and  $\gamma_2$ -phase as a function of time at 973 K under different dpa rates: (a) U-45 at% Nb and (b) U-25 at% Zr.

concentration. As the dose rate increases, the speed of spinodal decomposition decreases due to the atomic cascade mixing effect.

### 3.3 Effect of irradiation on the two-phase microstructure in U-Nb and U-Zr alloys

To study the effect of irradiation on the evolution of two-phase microstructure after spinodal decomposition, the two-phase microstructures of U-Nb and U-Zr alloys after spinodal decomposition for 1 h were applied as the initial state, and the simulated microstructure evolution of U-45 at% Nb and U-25 at% Zr alloys under irradiation were shown in Fig. 8 and 9, respectively. As can be seen from the figures, although the morphological orientation of two-phase structure does not change with time under irradiation, the equilibrium compositions of two phases are affected by the irradiation-induced cascade mixing. With the increase of irradiation time, the microstructure after spinodal decomposition gradually disappeared in U-45 at% Nb alloy under dpa rate of  $6 \times 10^{-4}$  dpa  $s^{-1}$  and U-25 at% Zr alloy under dpa rate of  $1 \times 10^{-4}$  dpa  $s^{-1}$ . The variations of compositions of two phases with time under irradiation in U-45 at% Nb and U-25 at% Zr alloys are shown in Fig. 10(a) and (b), respectively. It can be seen that the composition of the two phases gradually shift to the initial composition and then reach equilibrium values, leading to the decrease of miscibility gap width.

## 4. Discussion

In this work, a phase-field model coupled with cascade mixing and micro-elastic theory has been used to investigate the spinodal decomposition in U-Nb and U-Zr alloys. The results show that the elastic energy has an important influence on the orientation of the microstructure during the spinodal decomposition, and the irradiation-induced cascading mixing can affect the velocity of the spinodal decomposition and the

composition of the equilibrium state after decomposition. The microstructures and equilibrium compositions vary with the change of initial components in U-Nb and U-Zr.

In the above simulation, the elastic energy induced by the lattice misfit of the two phases was calculated during the spinodal decomposition. The isolated domains prefer to align in vertical and horizontal directions, which can be explained with the elastic anisotropy of the two alloy systems. It is well known that the elastic modulus can be defined as,<sup>58</sup>

$$E(\theta) = \left( \frac{C_{11} + C_{12}}{2} + \frac{C_{44}}{2\mu} \right) + 4C_{44} \left( 1 - \frac{1}{\mu} \right) \sin^2 \theta \cos^2 \theta \quad (15)$$

where  $\mu = 2C_{44}/(C_{11} - C_{12})$  is orientation factor. The curves of the variation of  $E$  as a function of the orientation in the U-45 at% Nb and U-25 at% Zr alloys are shown in Fig. 11(a) and (b). In the simulation, the stress free strain  $\varepsilon_{ij}^0$  of U-45 at% Nb and U-25 at% Zr alloys are chosen as 0.038 and 0.040.<sup>59</sup> It can be obviously seen from Fig. 1 and 2 that the overall spatial distribution of the isolated domains is interconnected rectangular stripes aligned in the  $\langle 10 \rangle$  crystallographic direction in order to reduce the elastic energy, which is in good agreement with the calculated results of elastic modulus shown in Fig. 11. The influence of elastic energy on the microstructure anisotropy of U-Nb alloy is greater than that of U-Zr alloy. With the increase of aging time, the microstructure after spinodal decomposition in U-Nb or U-Zr alloy gradually coarsens because of the Ostwald ripening. According to the simulation results of spinodal decomposition with different alloy composition under different irradiation intensities, it is obviously that the irradiation-induced cascade mixing has little effect on the morphology orientation of the separated two phases, but shows great influence on the equilibrium composition and volume fraction of the separated two phases.

According to the Fig. 2 and 6, the simulated microstructure morphology of U-Zr alloy after spinodal decomposition without irradiation is consistent of the experiment results studied by

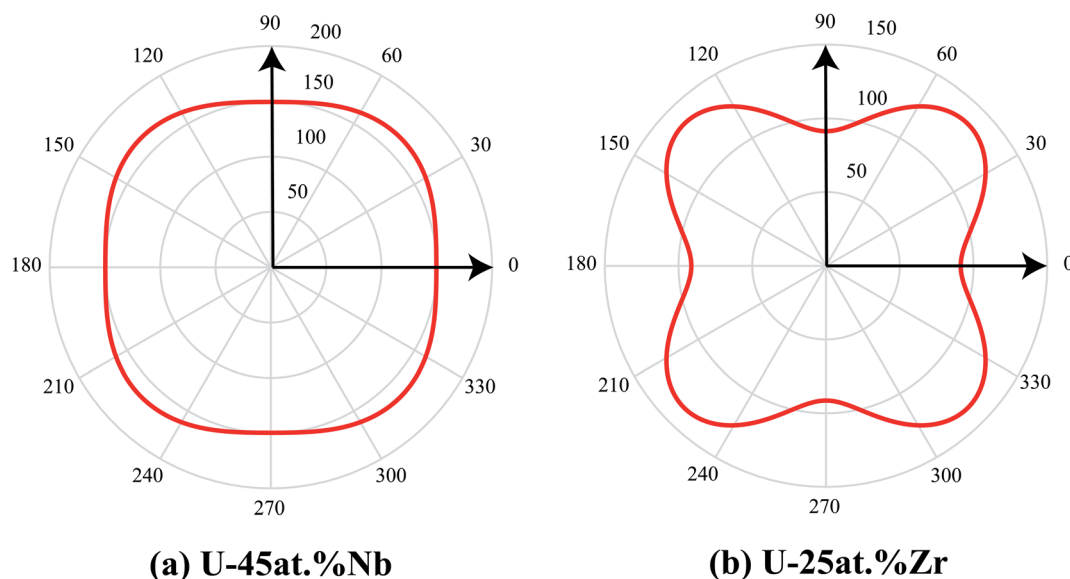


Fig. 11 Diagram of Young's modulus: (a) U-45 at% Nb and (b) U-25 at% Zr.



Yao *et al.* who investigated the U-50 wt% Zr spinodal microstructure and element distribution by *in situ* TEM annealing at 873 K for 30 min.<sup>60</sup> In Fig. 3 and 4, with the increase of dpa rate from 0 to  $6 \times 10^{-4}$  dpa s<sup>-1</sup>, equilibrium composition of  $\gamma_2$ -phase in U-45 at% Nb alloy decreases from 0.68 to 0.57 and the volume fraction of  $\gamma_2$ -phase decreases from 0.50 to 0.40. As the dpa rate increases from 0 to  $1 \times 10^{-4}$  dpa s<sup>-1</sup>,  $\gamma_2$ -phase of Zr equilibrium composition in U-25 at% Zr alloy decreases from 0.41 to 0.29 and the volume fraction of  $\gamma_2$ -phase increases from 0.42 to 0.52. The irradiation slows down the speed of the spinodal decomposition and reduces the amplitude of composition fluctuation. The increase of dose rates leads to the variation of equilibria composition in U-45 at% Nb and U-25 at% Zr alloys. In the U-Nb and U-Zr alloys, the volume fraction of  $\gamma_2$ -phase changes differently with the increase of dose rates. Under different irradiation conditions, the equilibria compositions of U-45 at% Nb are changed and the increase of dose rate inhibits solute enrichment, which leads to the decrease of the volume fraction of  $\gamma_2$ -phase in U-Nb alloy. The volume fraction of  $\gamma_2$ -phase in U-25 at% Zr alloy increases with the increase of dose rate, which indicate that the cascade mixing is able to strongly affect the process of spinodal decomposition.

With the increase of dose rates, the difference of the two equilibrium compositions ( $\Delta c^{\text{eq}}$ ) of spinodal decomposition in U-Nb and U-Zr alloys decreases dramatically. Without considering the irradiation, the metastable supersaturated solid solution will spontaneously decompose into two-phase mixtures with the same crystal structure by spinodal decomposition to reduce the free energy of the system. According to the simulation results, it can be seen that U-Nb alloy does not have the spinodal decomposition when the dpa rate reaches  $1.87 \times 10^{-3}$  dpa s<sup>-1</sup>, while the maximum dpa rate of U-Zr alloy which can undergo the spinodal decomposition is  $2.40 \times 10^{-4}$  dpa s<sup>-1</sup>. The ballistic effects oppose spinodal ordering according to Martin's results,<sup>61</sup> and the alloy does not undergo spinodal decomposition when the dose rate is large enough. Through the analysis of the above results, the time required for the alloy to decompose to the equilibrium state gradually increases with the increase of the dose rates. The irradiation-induced ballistic mixing causes a number of exchanges of atomic positions occur within a finite average relocation distance ( $R_L = 3.37 \times 10^{-10}$  m in U-Nb and  $R_L = 3.50 \times 10^{-10}$  m in U-Zr), which "re-mix" the local atom and makes the average composition of local atoms to a certain extent. In other words, irradiation-induced ballistic mixing acts in opposition to spinodal decomposition or demixing mechanism. Therefore, the spinodal decomposition of U-45 at% Nb and U-25 at% Zr alloys under irradiation is the competitive result of demixing and irradiation-induced ballistic mixing. Through the irradiation experiment on as-cast austenitic stainless steel, Fujii *et al.*<sup>62</sup> found that irradiation can reduce the fluctuation of solute composition and the degree of spinodal decomposition, which is consistent with our simulation results. The change of the equilibrium composition in  $\gamma_1$  and  $\gamma_2$ -phase at increasing dose rates is caused by more frequent cascade mixing replacement events, forcing the exchange of atoms from the matrix to precipitates and *vice versa*.<sup>33</sup> The simulation results of spinodal

decomposition under irradiation in U-Nb and U-Zr alloys are consistent with the different effect of cascade mixing in meso-scale phase field models by Schwen *et al.*<sup>63</sup> Their study demonstrated that the alloys exhibit obvious phase separation under low irradiation rates, and the degree of phase separation decreases with increasing irradiation rates. At sufficiently large irradiation rates, the alloys don't show phase separation and remain mixed. Thus, the irradiation-induced cascade mixing can slow the speed of spinodal decomposition and influences the equilibrium composition and volume fraction of the separated two phases in U-based alloys.

As can be seen from the Fig. 5–7, the U-50 at% Nb reaches the equilibrium composition much quicker than other U-Nb alloys, and the time to reach the equilibrium composition for the U-25 at% Zr is less than other U-Zr alloys. According to the thermodynamic database,<sup>7,8</sup> the U-50 at% Nb has the largest chemical driving force compared with other alloy components in U-Nb, while the chemical driving of U-25 at% Zr is stronger than other U-Zr alloys. At the temperature of 973 K, the diffusivity of U-50 at% Nb is  $1.51 \times 10^{-15}$  m<sup>2</sup> s<sup>-1</sup> and the initial composition of alloys changes so little that the diffusivity of U-Nb alloys does not change much. The diffusivity at 973 K of U-25 at% Zr is  $2.04 \times 10^{-15}$  m<sup>2</sup> s<sup>-1</sup>, and the change of composition in U-Zr alloys has little effect on the diffusivity under the same temperature. The influence of driving force during the spinodal decomposition is stronger than the effect of diffusivity, which leads to the less time to reach the equilibrium state for U-50 at% Nb and U-25 at% Zr alloys. The influence of irradiation on spinodal decomposition of different alloy composition shows that the greater driving force, the smaller effect of irradiation on the spinodal decomposition. Furthermore, the driving force of spinodal decomposition at 973 K for U-50 at% Nb alloy is larger than that of U-25 at% Zr alloy and irradiation has less effect on the spinodal decomposition of U-Nb alloy. The change of free energy with concentration was calculated based on the thermodynamic database,<sup>7,8</sup> the value of free energy decreases significantly with the increase of Nb concentration from 0.2 to 0.7, while the value of free energy increases gently with the increase of Zr concentration from 0.1 to 0.4. Under irradiation, due to the breaking of the original degree of order, the entropy of  $\gamma$ -phase can be increased, which leads to the decrease of the effective free energy in U-Nb and U-Zr alloys.<sup>64,65</sup> Under the influence of local cascade mixing, the effective free energy of Nb-lean phase decreases more than that of Nb-rich phase in U-Nb alloy, which leads to the volume fraction of Nb enriched phase decreases with the increase of dose rate. While the volume fraction of Zr enriched phase increases with the increase of dose rate because the effective free energy of Zr-rich phase decreases more than that of Zr-lean phase in U-Zr alloy. The volume fraction of Nb enriched phase decreasing in U-Nb alloy and the volume fraction of Zr enriched phase increasing in U-Zr alloy could be the various effect of driving force of spinodal decomposition and the decrease of effective free energy. Thus, the speed of spinodal decomposition and the equilibrium volume fraction of the  $\gamma_2$ -phase are influenced by the irradiation and the initial composition.





From Fig. 8–10, the forced cascade mixing can destabilize the  $\gamma_1$  and  $\gamma_2$ -phase precipitates by driving the Nb or Zr atoms back into solution. With the increase of the irradiation time, the microstructure of the alloys after the spinodal decomposition gradually disappeared until a new equilibrium state was reached. The largest composition difference appears at the interface of  $\gamma_1$  and  $\gamma_2$ -phase after spinodal decomposition. According to the equilibrium phase diagram,<sup>64</sup> the equilibrium concentration of Nb enriched phase after spinodal decomposition is 67.5% in U–Nb alloy. After long time aging, the concentration of Nb enriched phase decreases to 63.6% under the dpa rate of  $3.0 \times 10^{-4}$  dpa s<sup>-1</sup>, and the equilibrium concentration of Nb enriched phase decreases to 57.6% under the dpa rate of  $6.0 \times 10^{-4}$  dpa s<sup>-1</sup>. In the U–Zr alloy, the equilibrium concentration of Zr enriched phase after spinodal decomposition is 40.5% without irradiation,<sup>65</sup> while the equilibrium concentration of Zr enriched phase decreases to 35.9% under the dpa rate of  $5.0 \times 10^{-5}$  dpa s<sup>-1</sup>, and the equilibrium concentration of Zr enriched phase decreases to 29.2% under the dpa rate of  $1.0 \times 10^{-4}$  dpa s<sup>-1</sup>. According to Fig. 10, at 973 K, the width of the miscibility gap ( $\Delta c^{\text{eq}}$ ) is 0.36 under the dpa rate of  $3.0 \times 10^{-4}$  dpa s<sup>-1</sup> in U–Nb alloy, while the width of the miscibility gap decreases to 0.21 at the dpa rate of  $6.0 \times 10^{-4}$  dpa s<sup>-1</sup>. In U–Zr alloy, the width of the miscibility gap decreases from 0.21 to 0.09 with the increase of dpa rate from  $5.0 \times 10^{-5}$  dpa s<sup>-1</sup> to  $1.0 \times 10^{-4}$  dpa s<sup>-1</sup>. According to the simulated results of spinodal decomposition, the tendency of composition region to shrink in the present work coincides well with the previous thermodynamic calculation,<sup>64–66</sup> which shows that the miscibility gap shrinks with the effect of irradiation. Therefore, the atom mixing effect is most obvious at the interface at early stage and then causes the change of composition inside  $\gamma_1$  and  $\gamma_2$ -phase under irradiation. When the effect of irradiation-induced ballistic mixing and spinodal decomposition reaches an equilibrium state, and the compositions of the two phases no longer change.

## 5. Conclusion

In summary, the phase field method coupled with CALPHAD database and cascade mixing model have been employed to study the spinodal decomposition of U–Nb and U–Zr alloys under irradiation. The simulation results are helpful for understanding the spinodal decomposition in U–Nb and U–Zr alloys and the designing of metallic fuels working at high temperature and irradiation. It provides a new study on the behavior of U–Nb and U–Zr metallic nuclear fuels under neutron irradiation conditions with following results:

(1) The spinodal decomposition in U–Nb and U–Zr alloys could be inhibited with the increase of dose rates. The irradiation slows down the speed of the spinodal decomposition and reduces miscibility gap, which leads to the shrink of equilibria composition in U-45 at% Nb and U-25 at% Zr alloys.

(2) The volume fraction of  $\gamma_2$ -phase increases with increasing initial composition of Nb or Zr in U–Nb and U–Zr alloys under the same conditions. The dose rate shows great influence in the equilibria composition in U–Nb and U–Zr. With the increase of

dose rates, the volume fraction of Nb enriched phase in U–Nb alloy decreases after spinodal decomposition, while the volume fraction of Zr enriched phase in U–Zr alloy increases.

(3) When applying irradiation effect on the equilibrium two-phase microstructure of spinodal decomposition, the cascade mixing can destabilize the  $\gamma_1$  and  $\gamma_2$ -phase by driving the Nb or Zr atoms back into solution till the effect local cascade mixing and spinodal decomposition reach to a new equilibrium state.

## Conflicts of interest

There are no conflicts to declare.

## Acknowledgements

The authors would like to thank the financial support for this research by Natural Science Foundation of Fujian Province (2019J01033), National Key Research and Development Program of China (2017YFB0702401) and Fundamental Research Funds for the Central Universities (20720170038).

## References

- 1 D. E. Burkes, R. S. Fielding, D. L. Porter, D. C. Crawford and M. K. Meyer, *J. Nucl. Mater.*, 2009, **389**, 458–469.
- 2 B. S. Chandrasekhar and J. K. Hulm, *J. Phys. Chem. Solids*, 1958, **7**, 259–267.
- 3 T. C. Duong, R. E. Hackenberg, V. Attari, A. Landa, P. E. A. Turchi and R. Arróyave, *Comput. Mater. Sci.*, 2020, **175**, 109573.
- 4 K. Ghoshal, T. R. G. Kutty, S. Mishra and A. Kumar, *J. Nucl. Mater.*, 2013, **432**, 20–22.
- 5 L. C. Walters, *J. Nucl. Mater.*, 1999, **270**, 39–48.
- 6 G. L. Hofman, L. C. Walters and T. H. Bauer, *Prog. Nucl. Energy*, 1997, **31**, 83–110.
- 7 X. J. Liu, Z. S. Li, J. Wang and C. P. Wang, *J. Nucl. Mater.*, 2008, **380**, 99–104.
- 8 W. Xiong, W. Xie, C. Shen and D. Morgan, *J. Nucl. Mater.*, 2013, **443**, 331–341.
- 9 M. Paukov, I. Tkach, F. Huber, T. Gouder, M. Cieslar, D. Drozdenko, P. Minarik and L. Havela, *Appl. Surf. Sci.*, 2018, **441**, 113–119.
- 10 S. Kaity, J. Banerjee, S. C. Parida, P. G. Behere and V. Bhasin, *J. Nucl. Mater.*, 2020, **541**, 152427.
- 11 W. Chen and X.-M. Bai, *J. Nucl. Mater.*, 2018, **507**, 360–370.
- 12 A. J. Clarke, R. D. Field, R. E. Hackenberg, D. J. Thoma, D. W. Brown, D. F. Teter, M. K. Miller, K. F. Russell, D. V. Edmonds and G. Beverini, *J. Nucl. Mater.*, 2009, **393**, 282–291.
- 13 D. W. Brown, M. A. M. Bourke, A. J. Clarke, R. D. Field, R. E. Hackenberg, W. L. Hulst and D. J. Thoma, *J. Nucl. Mater.*, 2016, **481**, 164–175.
- 14 G. Bozzolo, H. O. Mosca, A. M. Yacout, G. L. Hofman and Y. S. Kim, *Comput. Mater. Sci.*, 2010, **50**, 447–453.
- 15 L. Hsiung and J. Zhou, *MRS Online Proceedings Library Archive*, 2005.



- 16 A. J. Clarke, R. D. Field, R. E. Hackenberg, D. J. Thoma, D. W. Brown, D. F. Teter, M. K. Miller, K. F. Russell, D. V. Edmonds and G. Beverini, *J. Nucl. Mater.*, 2009, **393**, 282–291.
- 17 T. Yao, A. R. Wagner, X. Liu, A. El-Azab, J. M. Harp, J. Gan, D. H. Hurley, M. T. Benson and L. He, *Materialia*, 2020, **9**, 100592.
- 18 T. Yao, L. Capriotti, J. M. Harp, X. Liu, Y. Wang, F. Teng, D. J. Murray, A. J. Winston, J. Gan, M. T. Benson and L. He, *J. Nucl. Mater.*, 2020, **542**, 152536.
- 19 G. Martin, *Phys. Rev. B: Condens. Matter Mater. Phys.*, 1984, **30**, 1424.
- 20 P. Wilkes, *J. Nucl. Mater.*, 1979, **83**, 166–175.
- 21 S. Hu, C. H. Henager, H. L. Heinisch, M. Stan, M. I. Baskes and S. M. Valone, *J. Nucl. Mater.*, 2009, **392**, 292–300.
- 22 S. Hu, D. E. Burkes, C. A. Lavender, D. J. Senor, W. Setyawan and Z. Xu, *J. Nucl. Mater.*, 2016, **479**, 202–216.
- 23 Y. Li, S. Hu, R. Montgomery, F. Gao and X. Sun, *Nucl. Instrum. Methods Phys. Res., Sect. B*, 2013, **303**, 62–67.
- 24 S. Y. Hu and C. H. Henager, *Acta Mater.*, 2010, **58**, 3230–3237.
- 25 X. Q. Ma, S. Q. Shi, C. H. Woo and L. Q. Chen, *Scr. Mater.*, 2002, **47**, 237–241.
- 26 X. Q. Ma, S. Q. Shi, C. H. Woo and L. Q. Chen, *Mech. Mater.*, 2005, **38**, 3–10.
- 27 X. H. Guo, S. Q. Shi, Q. M. Zhang and X. Q. Ma, *J. Nucl. Mater.*, 2008, **378**, 110–119.
- 28 X. H. Guo, S. Q. Shi, Q. M. Zhang and X. Q. Ma, *J. Nucl. Mater.*, 2008, **378**, 120–125.
- 29 K. Ahmed, J. Pakarinen, T. Allen and A. El-Azab, *J. Nucl. Mater.*, 2014, **446**, 90–99.
- 30 M. R. Tonks, Y. Zhang, X. Bai and P. C. Millett, *Mater. Res. Lett.*, 2014, **2**, 23–28.
- 31 Z. G. Mei, L. Y. Liang, Y. S. Kim, T. Wiencek, E. O'Hare, A. M. Yacout, G. Hofman and M. Anitescu, *J. Nucl. Mater.*, 2016, **473**, 300–308.
- 32 D. Gilles, D. Sylvain, L. Laurence, S. David and P. Vassilis, *Sci. Rep.*, 2018, **8**, 1–12.
- 33 J. Ke, E. R. Reese, E. A. Marquis, G. R. Odette and D. Morgan, *Acta Mater.*, 2019, **164**, 586–601.
- 34 A. G. Khachaturyan, *Theory of structural transformations in solids*, Courier Corporation, 2013.
- 35 Y. U. Wang, Y. M. Jin and A. G. Khachaturyan, *J. Appl. Phys.*, 2002, **92**, 1351–1360.
- 36 Z. W. Yan, S. J. Shi, Y. S. Li, J. Chen and M. Shahid, *Phys. Chem. Chem. Phys.*, 2020, **22**, 3611–3619.
- 37 J. W. Cahn, *J. Chem. Phys.*, 1965, **42**, 93–99.
- 38 J. W. Cahn and J. E. Hilliard, *J. Chem. Phys.*, 1958, **28**, 258–267.
- 39 A. T. Dinsdale, *Calphad*, 1991, **15**, 317–425.
- 40 Y. Lu, Q. Q. Tang, C. P. Wang, Z. S. Li, Y. H. Guo and X. J. Liu, *J. Phase Equilib. Diffus.*, 2018, **39**, 714–723.
- 41 J. O. Andersson and J. Ågren, *J. Appl. Phys.*, 1992, **72**, 1350–1355.
- 42 B. Bian, P. Zhou, S. Wen and Y. Du, *Calphad*, 2018, **61**, 85–91.
- 43 Y. Park, R. Newell, A. Mehta, D. D. Keiser and Y. H. Sohn, *J. Nucl. Mater.*, 2018, **502**, 42–50.
- 44 R. A. Enrique and P. Bellon, *Phys. Rev. Lett.*, 2000, **84**, 2885.
- 45 P. E. L'vov and V. V. Svetukhin, *Modell. Simul. Mater. Sci. Eng.*, 2021, **29**, 035013.
- 46 R. A. Enrique and P. Bellon, *Phys. Rev. B: Condens. Matter Mater. Phys.*, 2001, **63**, 134111.
- 47 P. Bellon, *Materials Science with Ion Beams*, 2009, pp. 29–52.
- 48 M. J. Norgett, M. T. Robinson and I. M. Torrens, *Nucl. Eng. Des.*, 1975, **33**, 50–54.
- 49 G. Martin and P. Bellon, *Solid State Phys.*, 1996, **50**, 189–331.
- 50 R. S. Averback and T. D. D. L. Rubia, *Solid State Phys.*, 1997, **51**, 281–402.
- 51 Y. H. Wen, J. P. Simmons, C. Shen, C. Woodward and Y. Wang, *Acta Mater.*, 2003, **51**, 1123–1132.
- 52 B. Beeler, C. Deo, M. Baskes and M. Okuniewski, *J. Nucl. Mater.*, 2013, **433**, 143–151.
- 53 B. T. Wang, P. Zhang, H. Y. Liu, W. D. Li and P. Zhang, *J. Appl. Phys.*, 2011, **109**, 063514.
- 54 Z. H. Liu and J. X. Shang, *Chin. Phys. B*, 2012, **21**, 357–362.
- 55 J. W. Cahn and J. E. Hilliard, *J. Chem. Phys.*, 1959, **31**, 688–699.
- 56 K. Nordlund, S. J. Zinkle, A. E. Sand, F. Granberg, R. S. Averback, R. E. Stoller, T. Suzudo, L. Malerba, F. Banhart, W. J. Weber, F. Willaime, S. L. Dudarev and D. Simeone, *J. Nucl. Mater.*, 2018, **512**, 450–479.
- 57 R. A. Enrique, K. Nordlund, R. S. Averback and P. Bellon, *J. Appl. Phys.*, 2003, **93**, 2917–2923.
- 58 Y. H. Wang, D. C. Zhang, Z. P. Pi, J. G. Lin and C. Wen, *J. Appl. Phys.*, 2019, **126**, 085102.
- 59 Y. S. Li, Y. Z. Yu, X. L. Cheng and G. Chen, *Mater. Sci. Eng., A*, 2011, **528**, 8628–8634.
- 60 T. Yao, A. Sen, A. Wagner, F. Teng, M. Bachhav, A. El-Azab, D. Murray, J. Gan, D. H. Hurley, J. P. Wharry, M. T. Benson and L. He, *Materialia*, 2021, **16**, 101092.
- 61 G. Martin, *Phys. Rev. B: Condens. Matter Mater. Phys.*, 1984, **30**, 1424.
- 62 K. Fujii and K. Fukuya, *J. Nucl. Mater.*, 2013, **440**, 612–616.
- 63 D. Schwen, S. Schunert and A. Jokisaari, *Comput. Mater. Sci.*, 2021, **192**, 110321.
- 64 X. J. Liu, Y. L. Zhao, Y. Lu, W. W. Xu, J. P. Jia and C. P. Wang, *J. Nucl. Mater.*, 2014, **451**, 366–371.
- 65 Y. Lu, Z. Jiang, L. Y. Li, C. P. Wang, Y. H. Guo, J. J. Han and X. J. Liu, *J. Nucl. Eng. Radiat. Sci.*, 2021, **7**, 011605.
- 66 C. Abromeit, H. Wollenberger, S. Matsumura and C. Kinoshita, *J. Nucl. Mater.*, 2000, **276**, 104–113.

